

Galactic ^{26}Al traces metal loss through hot chimneys

Martin G. H. Krause^{1*}, Donna Rodgers-Lee², James E. Dale¹, Roland Diehl³
and Chiaki Kobayashi¹

¹*Centre for Astrophysics Research, Department of Physics, Astronomy and Mathematics, University of Hertfordshire, College Lane, Hatfield, Hertfordshire AL10 9AB, UK*

²*School of Physics, Trinity College Dublin, University of Dublin, College Green, Dublin 2, D02 PN40, Ireland*

³*Max-Planck-Institut für extraterrestrische Physik, Giessenbachstrasse 1, Garching D-85748, Germany*

Accepted XXX. Received YYY; in original form ZZZ

ABSTRACT

Radioactive ^{26}Al is an excellent tracer for metal ejection in the Milky Way, and can provide a direct constraint on the modelling of supernova feedback in galaxy evolution. Gamma-ray observations of the ^{26}Al decay line have found high velocities and hence require a significant fraction of the Galactic ^{26}Al in the hot component. At the same time, meteoritic data combined with simulation results suggest that a significant amount of ^{26}Al makes its way into stars before decay. We investigated the distribution into hot and cold channels with a simulation of a Milky-Way-like galaxy with massive-star feedback in superbubbles and with ejecta traced by ^{26}Al . About 30–40 per cent of the ejecta remain hot, with typical cooling times of the order Gyr. ^{26}Al traces the footpoints of a chimney-fed outflow that mixes metals turbulently into the halo of the model galaxy on a scale of at least 50 kpc. The rest diffuses into cold gas $\lesssim 10^4$ K, and may therefore be quickly available for star formation. We discuss the robustness of the result by comparison to a simulation with a different global flow pattern. The branching ratio into hot and cold components is comparable to that of longer term average results from chemical evolution modelling of galaxies, clusters and the intracluster medium.

Key words: gamma-rays: ISM – ISM: abundances – ISM: bubbles – hydrodynamics – meteorites, meteors, meteoroids – galaxies: abundances

1 INTRODUCTION

Observations of galaxy clusters and the intracluster medium (Böhlinger & Werner 2010; Renzini & Andreon 2014; Simionescu et al. 2019), as well as analysis of metals in stars and the interstellar and circumgalactic medium (Maiolino & Mannucci 2019, and references therein), suggest that the majority of metals produced in stars probably leaves the galaxies and enriches the circum-/intergalactic medium. The argument is made globally, analysing mass budgets of either the intracluster medium, or late populations of stars that have been enriched by many preceding generations of stars over many Gyr. Chemodynamical cosmological simulations relate the fraction of metals not quickly recycled in stars to the strength of feedback in the galaxy, and predict that this fraction is higher for lower-mass galaxies (e.g., Kobayashi, Springel & White 2007; Taylor & Kobayashi 2015).

These extragalactic findings have an important complement in direct observations of the ejecta in the Milky Way, where we can trace their path in gamma rays with radioactive elements ejected from stars together with the stable elements. Since chemical elements generally form in stars, radioactive elements are a reliable way to identify recent stellar ejecta. Isotopes with different decay times trace ejecta from timescales of weeks (^{56}Ni , Diehl et al. 2014) through centuries

(^{44}Ti , Iyudin et al. 1994; Renaud et al. 2006) and Myr (^{26}Al and ^{60}Fe , Diehl et al. 1995; Knie et al. 2004; Wang et al. 2007, 2020), up to 10^8 yr (^{244}Pu , Wallner et al. 2015).

^{26}Al ($\tau = 1$ Myr) has been observed to be present throughout the Milky Way, via the 1.8 MeV radioactive decay line (Prantzos & Diehl 1996; Plüschke et al. 2001; Diehl et al. 2006; Bouchet et al. 2015). The appearance of diffuse but clumpy ^{26}Al emission along the entire band of the Milky Way has been used to argue that ^{26}Al is emitted mainly by massive stars (Prantzos & Diehl 1996). These represent a young stellar population, which is forming currently in the disc of the Galaxy, rather than in the bulge. ^{26}Al enters the interstellar medium with hot gas ejected in fast ($\gtrsim 1000$ km s $^{-1}$) winds and supernova explosions (Prantzos & Diehl 1996; Diehl 2013). The radioactive decay effectively attaches a clock to the ejected ^{26}Al . High-resolution spectroscopy of the ^{26}Al gamma-ray line with the spectrometer onboard the INTEGRAL satellite has found Doppler shifts and line broadenings. Through this, discrimination is obtained of the dominant gas phase that the nuclei reside in at the time of their decay (Kretschmer et al. 2013). The high velocities found are evidence for a significant part of the Galactic ^{26}Al production occurring and remaining in the hot phase $\approx 10^6$ years after ejection (Krause et al. 2015).

High abundances of ^{26}Mg , the decay product of ^{26}Al , have been found in early-formed parts of meteorites (MacPherson et al. 2010; Groomman et al. 2015). This suggests the inclusion of very recent

* E-mail: M.G.H.Krause@herts.ac.uk

massive star ejecta in the material from which the solar system formed (e.g., Gounelle 2015; Lugaro et al. 2018, and references therein). ^{26}Al also may have played an important role in heating the protoplanetary disc of the solar nebula, with a major impact on ice melting and evaporation and hence the abundance of water, crucial for the habitability of rocky planets (Lichtenberg et al. 2019). It is debated if the ^{26}Al abundance in the early solar system was very special or if it is a rather typical case (e.g., Dwarkadas et al. 2017; Portegies Zwart 2019). If it was typical, as recently argued from 3D hydrodynamic simulations by Fujimoto et al. (2018), this would indicate that also a significant part of massive-star ejecta might be incorporated into new stars before ^{26}Al has decayed, and hence a rapid re-cycling time for this fraction of the massive-star ejecta.

The study of chemical evolution in galaxies and the intracluster medium thus leads us to a similar picture as the ^{26}Al gamma-ray observations and the data from the early solar system: high fractions of massive star ejecta need on the one hand to be mixed into the dense, star-forming interstellar medium locally and on the other hand to remain in hot gas to be able to be ejected from the galaxy. Propagation of ejecta and mixing of different phases of the interstellar medium can be studied in three-dimensional hydrodynamics simulations (e.g., Breitschwerdt et al. 2016; Krause et al. 2018). Separate whole-galaxy simulations have recently demonstrated that both, the Milky Way's ^{26}Al gamma-ray emission (Rodgers-Lee et al. 2019) and the amount of ^{26}Al in dense, star-forming gas can be reproduced, with the abundance level of the solar system as a likely outcome (Fujimoto et al. 2018). Here, we now demonstrate explicitly with representative simulations that comparable fractions of massive-star ejecta traced by ^{26}Al are indeed found in cold and hot gas, respectively, and that ^{26}Al in the hot gas is located in the launch region of outflows through chimneys that reach tens of kpc into the halo. Because ^{26}Al is a good tracer of massive star ejecta in general, this has implications for all massive-star ejecta. We first review ejection, propagation and mixing of stellar ejecta in Sect. 2, then describe the simulation in Sect. 3 with results in Sect. 4. We discuss our results on the background of complementary work in Sect. 5 and summarise our conclusions in Sect. 6.

2 THE PATH OF MASSIVE STAR EJECTA

Models predict that ^{26}Al may be ejected during the main-sequence or Wolf-Rayet phase of a single or binary massive star (Gounelle & Meynet 2012; Brinkman et al. 2019), and in supernovae (Limongi & Chieffi 2006; Woosley & Heger 2007; Nomoto et al. 2013). The explosive contribution can be addressed with the isotopic ratio $^{60}\text{Fe}/^{26}\text{Al}$, where ^{60}Fe has a decay time of 4 Myr and is thought to be produced in supernovae, only. ^{60}Fe is found in deep sea sediments, suggesting a relatively nearby supernova 2-3 Myr ago (Feige et al. 2018). The non-detection of ^{26}Al would constrain the $^{60}\text{Fe}/^{26}\text{Al}$ ratio for this supernova to > 0.18 , well consistent with expectations of ≈ 2 (Austin et al. 2017). INTEGRAL observations of the interstellar medium find $^{60}\text{Fe}/^{26}\text{Al}=0.2-0.4$ (Wang et al. 2020), which suggests a significant or even dominant non-supernova contribution.

Massive stars form in groups and clusters (Zinnecker & Yorke 2007), and quickly ionise their surroundings, producing parsec-scale HII regions on a timescale of 10^5 yr (Mackey et al. 2015). Massive star winds then energise and heat the interior of bubbles of the order of 10 pc to X-ray temperatures $\approx 10^6$ yr after star formation (e.g. Weaver et al. 1977; Churchwell et al. 2006; Everett & Churchwell 2010; Krause et al. 2013, 2014). The clustering of massive stars implies the formation of superbubbles (e.g. Oey & Garca-Segura

2004; Breitschwerdt & de Avillez 2006; Jaskot et al. 2011; Sasaki et al. 2011; Krause et al. 2013, 2018; Schulreich et al. 2018).

After being expelled from their sources, the massive-star ejecta are shocked to high temperatures within these bubbles (e.g., Krause et al. 2013, their Fig. 6). Then they gradually mix trans-sonically, through turbulence and instabilities, on the sound crossing timescale into the hot gas throughout the entire superbubble (Breitschwerdt et al. 2016; Krause et al. 2018). Observations point to efficient turbulent mixing between hot and cold gas: Without such mixing, the superbubbles would be too hot (Dunne et al. 2001) and would grow too quickly (e.g. Oey & Garca-Segura 2004). High-resolution 3D hydrodynamics simulations have shown that a turbulent mixing zone between the hot interior and the shell arises naturally via instabilities due to the time-dependent nature of the energy supply. This dissipates the bulk of the energy, and ensures realistic bubble growth (Krause & Diehl 2014). Entrainment of cold shell gas cools the superbubble interior to temperatures around or just below 1 keV and enhances the luminosities, both in good agreement with observations (Krause et al. 2014). Mixing is strongest just after supernova explosions, thus explaining the Myr timescale X-ray variability of superbubbles (Krause & Diehl 2014). Other processes that mix massive star ejecta with dense gas include ablation of clouds enclosed in the hot bubbles (Rogers & Pittard 2013). Hot, ejecta-enriched gas surrounds such clouds (Gaczowski et al. 2015, 2017), squashing them because of pressure differences which may induce the formation of stars (Krause et al. 2018).

Fujimoto et al. (2018) followed the diffusion of ^{26}Al ejected by massive stars in a 3D hydrodynamic simulation of a whole galaxy and found that the range of inferred isotopic ratios of ^{26}Al to stable ^{27}Al in self-consistently formed stars was in good agreement with values from solar system meteorites, implying that the Sun was a typical star. They also show that most of their ^{26}Al is found in the cold phase, with 56 per cent of the total mass being in molecular clouds. Pleintinger et al. (2019) have compared their simulation results to the gamma-ray data, and found that the simulation could not account for the high observed scale heights of ^{26}Al in the Milky Way. They concluded that star formation in the simulation was likely too fine-grained, possibly due to the neglect of prominent spiral arms. It appears possible that this may have led to enhanced interaction between the gas phases in that simulation, and an overestimate of ^{26}Al in the star-forming gas. More recently, Fujimoto et al. (2020) have followed up on this with new simulations. They show that material spiral arms that form spontaneously from self-gravity in the disc also cannot solve the scale-height problem and suggest instead that the Sun is at a special place where foreground dominates the ^{26}Al signal. While there is some evidence for material arms, the exact nature of the spiral arms of the Milky Way is still debated (e.g., Sellwood et al. 2019; Pettitt et al. 2020, see Fujimoto et al. (2020) for more discussion).

Rodgers-Lee et al. (2019) performed similar simulations (details below), but with a more coarsely-grained star formation prescription than that of Fujimoto et al. (2018). They imposed spiral arms by an external potential. Comparing to gamma ray observations of ^{26}Al , they generally found good agreement, but some discrepancy regarding the kinematic structure. While the latter cannot be reproduced in detail, possibly because details of star formation in spiral arms are not taken into account accurately enough, they show that velocities comparable to the observed ones (different from the cold gas) are present in the simulation.

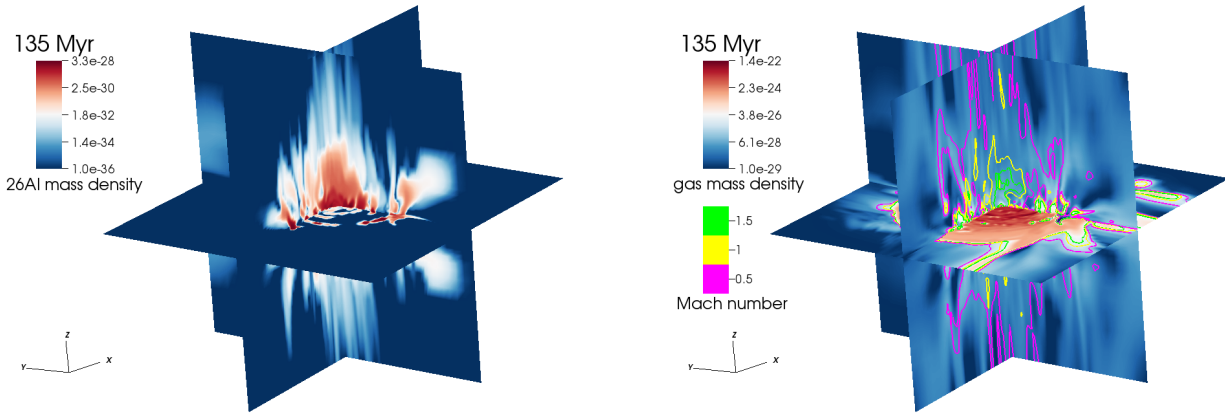


Figure 1. 3D renderings of run LoH+ at 135 Myr. Both visualisations extend 20 kpc from the centre of the simulated galaxy along each axis in positive and negative directions. Left: ^{26}Al density. ^{26}Al streams off from the disc to significant scale height. Right: Density with contours of the Mach number at 0.5, 1 and 1.5. ^{26}Al marks the base of a larger outflow. Movies are available with the online version of the journal.

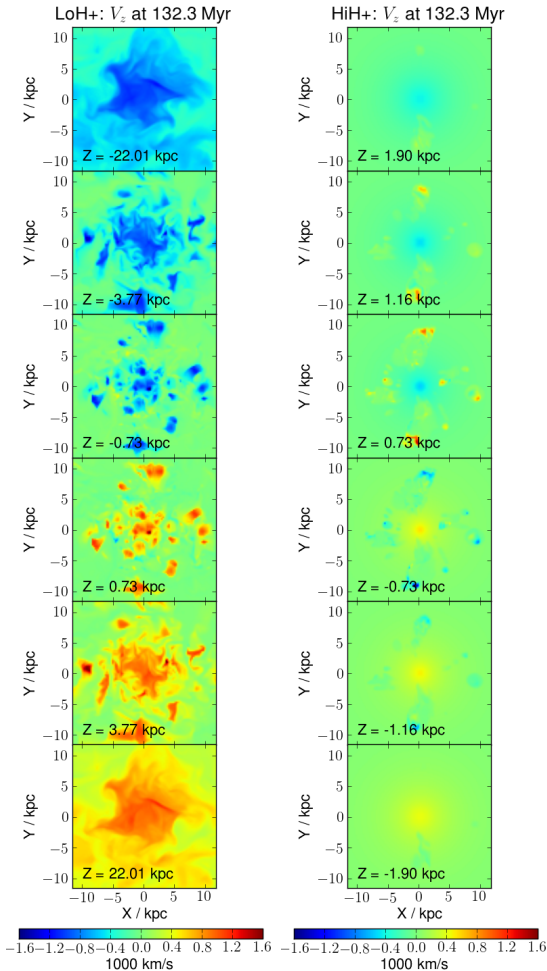


Figure 2. Halo flow pattern for the two simulations analysed. Shown is the velocity vertical to the disc at different altitudes indicated in the individual panels. Run LoH+ (left) with an observationally constrained halo density develops fast winds locally, that ascend in chimneys and have turned subsonic by 20 kpc above the disc. This turbulent flow extends beyond the simulation box (100 kpc each way). Run HiH+ (right) with higher halo density develops a convection zone of $\approx 1 - 2$ kpc extent around the galactic disc.

3 SIMULATIONS

The simulation we analyse here have been presented in detail in [Rodgers-Lee et al. \(2019\)](#). In short, it is a set of 3D hydrodynamic simulations of the interstellar medium of an isolated disc galaxy set in a gravitational potential that represents the static dark matter halo, stellar bulge, disc and rotating spiral arms. Superbubbles representing star forming regions of $10^6 M_\odot$ were injected at predetermined positions near spiral arms with energy, mass and ^{26}Al mass equivalent to a state at 10 Myr after star formation. The parameters for the gravitational potential, the disc size and the star formation rate were chosen to resemble the Milky Way¹. Standard optically thin cooling down to 10^4 K was implemented, where the gas was assumed to be kept ionised by ultraviolet radiation of stars. Radiative cooling below 10^4 K was not allowed, but such gas can still cool via adiabatic expansion. In [Rodgers-Lee et al. \(2019\)](#) we presented several simulations where the position of the superbubbles relative to the ridge line of the spiral arms had been varied as well as the density of the hydrostatic gas halo. For the present analysis, we verified that the results do not depend on the details of the positioning of the superbubbles with respect to the spiral arms and we only show results from the simulations with the superbubbles offset towards the leading edges of the spiral arms.

As we show below, the simulation with the observationally constrained lower central halo gas density of $4.4 \times 10^{-28} \text{ g cm}^{-3}$ (run LoH+ in the following) develops a patchy, chimney-like wind structure that transitions to subsonic flow at high altitudes above and below the disc (Fig. 1), whereas the one with a central density of $1.8 \times 10^{-25} \text{ g cm}^{-3}$ (run HiH+ in the following) develops no large-scale convection beyond a few kpc. The halo density in run HiH+ is unrealistically high. We include it here to show that even for this strong variation of the halo density and resulting flow structure, the

¹ We have become aware of a factor of two error in the energy injection rate, which means that the energy injection in these simulations corresponded to a star formation rate of $6 M_\odot \text{ yr}^{-1}$ rather than $3 M_\odot \text{ yr}^{-1}$. For the present paper, we have re-run a representative simulation (lower density halo, superbubbles offset towards the leading edge, ‘LoH+’) with the correct energy input rate. This reduces the scale height of ^{26}Al somewhat, but otherwise does not lead to a significant change of the results, in particular the predictions for the observed ^{26}Al kinematics. We use the new LoH+ run in the present paper but keep the original comparison run with high halo density (‘HiH+’).

changes to the branching ratio of ^{26}Al diffusing into, respectively, hot and cold gas are moderate.

4 RESULTS

We demonstrate the difference for the flow pattern of the two simulations in Fig. 2. There are two basic hydrodynamic flow patterns for galaxy halos, supersonic winds (Chevalier & Clegg 1985) and lower halo convection (de Avillez & Breitschwerdt 2004). The observational threshold for formation of winds in star-forming galaxies is around a star formation rate density of $0.1 M_{\odot} \text{ yr}^{-1} \text{ kpc}^{-2}$ (Heckman et al. 2015). This agrees well with the onset of winds in similar simulations where stellar feedback is implemented in the form of superbubbles (von Glasow et al. 2013). We have used a star formation rate of $3 (6) M_{\odot} \text{ yr}^{-1}$ for run LoH+ (HiH+). So, averaged over the whole disc the star formation rate density is $0.01 (0.02) M_{\odot} \text{ yr}^{-1} \text{ kpc}^{-2}$, well below the threshold for wind formation. Locally, for each implemented superbubble, the star formation rate density is $0.04 (0.08) M_{\odot} \text{ yr}^{-1} \text{ kpc}^{-2}$. This comes close enough to the threshold, so that marginally supersonic outflows are launched in our simulations locally from each superbubble (Fig. 3). These outflows contain hot gas $\gtrsim 10^6 \text{ K}$, only (Fig. 4), and would therefore not be expected to show up in ultraviolet wind studies such as the one of (Heckman et al. 2015). In run LoH+, these outflows rise conically, vertically away from the disc. About 20 kpc above and below the disc, the cones have merged and decelerated to a subsonic flow. The flow then streams out of our simulation box at 100 kpc. In run HiH+, the high density of the halo chokes the outflows and the circulation is restricted to a $\approx 2 \text{ kpc}$ region around the disc (Fig. 2, right).

We show midplane slices of the density of ^{26}Al nuclei in Fig 5 for run LoH+. A movie is provided with the online version of the journal. The superbubbles form long-lasting cavities that are repeatedly filled with ^{26}Al -rich ejecta. They are advected into the halo in chimneys, where radioactive decay limits the scale height achieved by the ejecta. This can be seen more clearly in the two-dimensional slices of the phase space density of the ^{26}Al nuclei shown in Fig. 6. We show the $z - v_z$ -slice, where z denotes the vertical coordinate, for both simulations. For run LoH+, we find large outflow velocities in excess of 1000 km/s for the ^{26}Al nuclei. At these velocities, ^{26}Al advances by 1-2 kpc per decay time. The decay is clearly visible along the inner 7 kpc of the outflow. In contrast, the ejecta in run HiH+ are limited by the dense halo. Only a small fraction of the ejecta acquires velocities above 500 km/s, and only near the launch point of the outflows.

The temperature distribution by mass fraction for ^{26}Al is compared to the one for all gas for representative snapshot times in Fig. 7. The distribution for ^{26}Al has some variation in time. Overall, there is a marked difference to the general gas distribution. This is true for the low density run LoH+, where the hot halo (inside our simulated box) contributes only a few per cent of the overall baryonic mass, as well as in run HiH+, where it contributes around 90 per cent. In run LoH+, a significant fraction of the ^{26}Al mass remains at high temperatures with typically 30-40 per cent above 10^6 K . This fraction decreases to 20 per cent for run HiH+.

The ^{26}Al in the cold component is likely to quickly find its way into new stars. For the hot one, a typical timescale is given by the radiative cooling timescale. To obtain a lower limit for the radiative cooling time t_c , we assume solar metallicity and use the collisional ionisation equilibrium cooling curve of Sutherland & Dopita (1993), $\Lambda(T)$, $t_c = k_B T / (n \Lambda)$, where k_B is the Boltzmann constant and n is the particle density. We show the cooling time distributions for

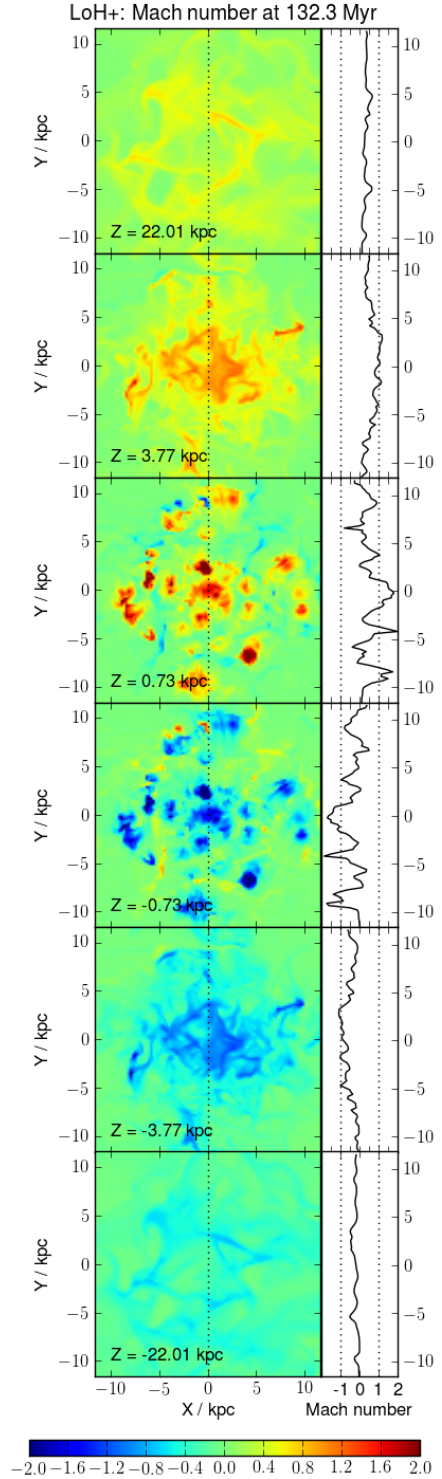


Figure 3. Maps and cross sections of the vertical Mach number for various slices above and below the disc midplane for run LoH+. The altitude is given in the individual panels. A dotted line in the maps at each altitude denotes the location for the cross section shown on the right of each map. In the latter plots, two dashed lines indicate Mach numbers of one in upward (positive) and downward (negative) directions, respectively.

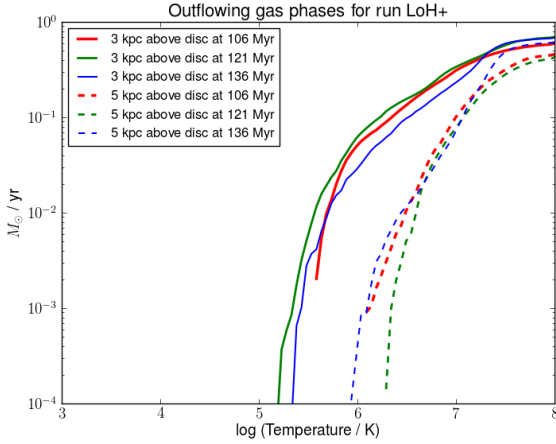


Figure 4. Cumulative temperature histograms weighted with the outflowing mass flux for a circular cross section of 9 kpc radius 3 and 5 kpc above the disc for run LoH+. Only outflowing gas is taken into account. We find no outflowing gas below 10^5 K. Gas with $10^5 - 10^6$ K falls back to the disc before reaching 5 kpc altitude. From then on, only gas with at least 10^6 K is present in the outflow.

hot gas with temperature $T > 10^6$ K that carries ^{26}Al in Fig 8. The median for run LoH+ is a few Gyr. Less than about 10 per cent of the ^{26}Al mass is associated with gas that can cool on the dynamical timescale of a galaxy (~ 100 Myr). For run HiH+, the cooling time distribution becomes more variable. The median is typically just below a Gyr, and the fraction of ^{26}Al -traced gas that can cool on a dynamical timescale of the galaxy varies between a few and above 30 per cent.

5 DISCUSSION

Our simulations do not include the first 10 Myr of star formation. This is a reasonable approximation for the study of large scale interstellar medium dynamics, because it is well-known that the embedded phase of star formation lasts at most a few Myr, and that most of the ^{26}Al (and other metals) are ejected into large superbubbles. This is especially true for supernova ejecta.

It is interesting in this context to compare our results to Fujimoto et al. (2018), who model the physics of star formation in much more detail, but do not include spiral arms in their simulations. They find that a significant fraction of ^{26}Al ends up in the next generation of stars, being mixed on the ^{26}Al decay timescale. In typical stars, the predicted isotopic ratio $^{26}\text{Al}/^{27}\text{Al}$ is therefore reduced by about one order of magnitude, only, from the average interstellar medium value, which had been determined from gamma-ray surveys to be $\approx 5 \times 10^{-4}$ (Diehl 2013). The Sun, with an initial value of $\approx 5 \times 10^{-5}$ would therefore be a rather typical star. Our simulation makes very different assumptions about the spatial arrangement of stellar feedback. We impose spiral arms, ignore the first 10 Myr after star formation, and instead inject superbubbles at this stage with a diameter of 600 pc. We still find in our simulation results that at least half of the ^{26}Al by mass diffuses into the cold phase. The agreement between the two simulations suggests that for the scales studied here, mixing does not strongly depend on small-scale details unresolved in our simulations and that we capture mixing reasonably well.

For our main run LoH+, ^{26}Al in the hot phase traces a fraction of about 30-40 per cent of the massive star ejecta that diffuse out

of the galaxy into its gaseous halo. The outflow is hot (Fig. 4) and can be seen directly in Figs. 1, 5 and 6. Typical cooling times are of the order of Gyr. This identifies a component of interstellar gas that characterises the enrichment of the circumgalactic and possibly intergalactic medium. Even in the simulation with unrealistically high halo density (HiH+), this fraction is reduced by a factor of two, only. It thus gives us a robust limit for the branching ratio of ^{26}Al in hot and cold gas at the time of its decay.

The occurrence of the outflow depends strongly on the assumed halo density. In contrast to the higher halo density simulation, the lower halo density run produced the outflow even though it had a lower star-formation rate. The outflow occurs somewhat below the observational threshold for the star-formation rate surface density from winds detected in the ultraviolet band (compare Sect. 4). Our outflow is, however, too hot to be detected in this way and would instead require sensitive high-resolution spectroscopy in X-rays to be observed.

Apart from this hot outflow from our inter-arm regions, the interstellar medium dynamics in our simulations are similar to other theoretical work and observations of disc galaxies. We show this here with the velocity dispersion and the Toomre (1964) Q parameter, which have been used in the literature to characterise structure and dynamics of the interstellar medium in disc galaxies (e.g., Krumholz et al. 2018; Orr et al. 2020). Krumholz et al. (2018) show that the Toomre stability parameter may be expressed as:

$$Q = \frac{f\kappa\sigma}{\pi G\Sigma_g},$$

where $\sigma = \sqrt{3\sigma_z^2 + c_s^2}$ represents the total gas velocity dispersion including bulk and thermal motions. c_s is the speed of sound, κ the epicyclic frequency, Σ_g the gas surface density and f a factor that takes into account that the gas surface density rather than the total gravitating density is used. We follow Krumholz et al. (2018) and adopt $f = 0.5$. $Q \approx 1$ is expected for a star-forming disc galaxy. Figure 9 displays the distribution of the Toomre Q parameter for the disc region (cylindrical radius less than 9 kpc, altitude above (below) the disc less than 0.5 kpc) for run LoH+ towards the end of the simulation as a function of gas temperature. Most of the cold material indeed assembles around $Q \approx 1$. We show the run of the mass-weighted Q -parameter over time in Fig. 10. Q is mostly between two and three for the part of the simulation we evaluate.

We also calculate the mass-weighted line-of-sight velocity dispersion vertical to the disc, σ_z , for the same disc region as before. It is also plotted against time in Fig. 10. For the late times that we are interested in here, the velocity dispersion has converged to about 7 km s^{-1} . This can be compared to dense gas tracers for which recent simulations and observations find values in the range of 5-30 km s^{-1} (Das et al. 2020; Orr et al. 2020).

We conclude that the parameters that characterise the dynamics of the interstellar medium in our simulated galaxies are, overall, realistic. In particular, there is no evidence for enhanced vertical motion of dense gas that would conflict with observations of star-forming galaxies.

Over cosmological timescales, if the metals accumulate in the halo, the cooling time would continuously decrease until the gas would eventually cool and form stars. However, halo gas can also be lost from a galaxy, for example because of Active Galactic Nucleus (AGN) feedback (Taylor & Kobayashi 2015). In particular, similar to processes believed to take place in galaxy clusters, radio AGN can produce buoyant bubbles that can drag a large fraction of inner halo gas in their wake (Heath, Krause & Alexander 2007). Despite radio AGN being principally observed in galaxy clusters they could

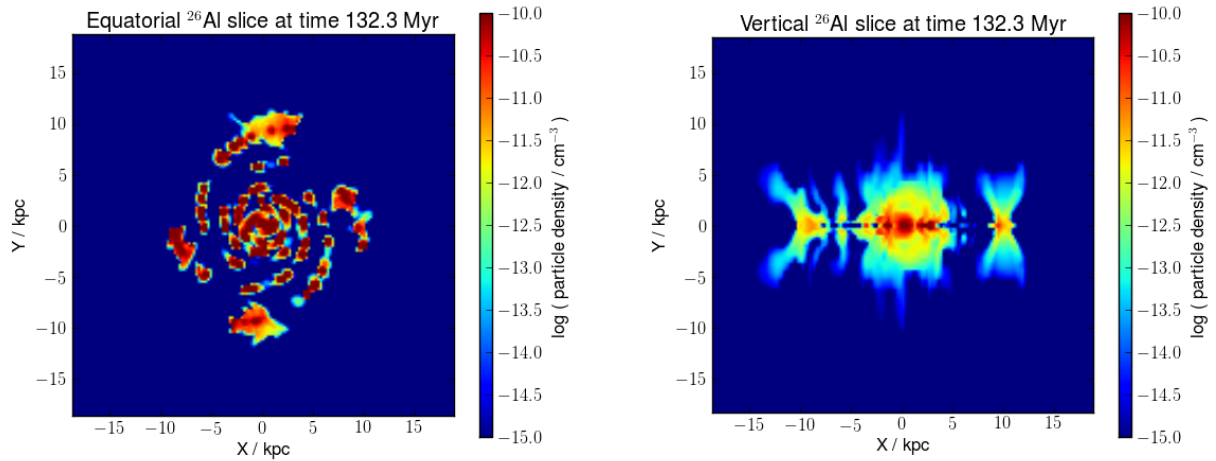


Figure 5. Slice through the equatorial midplane (left) and a vertical midplane (right) for run LoH+ at 132.3 Myr. We show the density of ^{26}Al nuclei. ^{26}Al fills long-lasting cavities with repeated cycles of injection, advection out of the galactic plane and decay. A movie is provided with the online version of the journal.

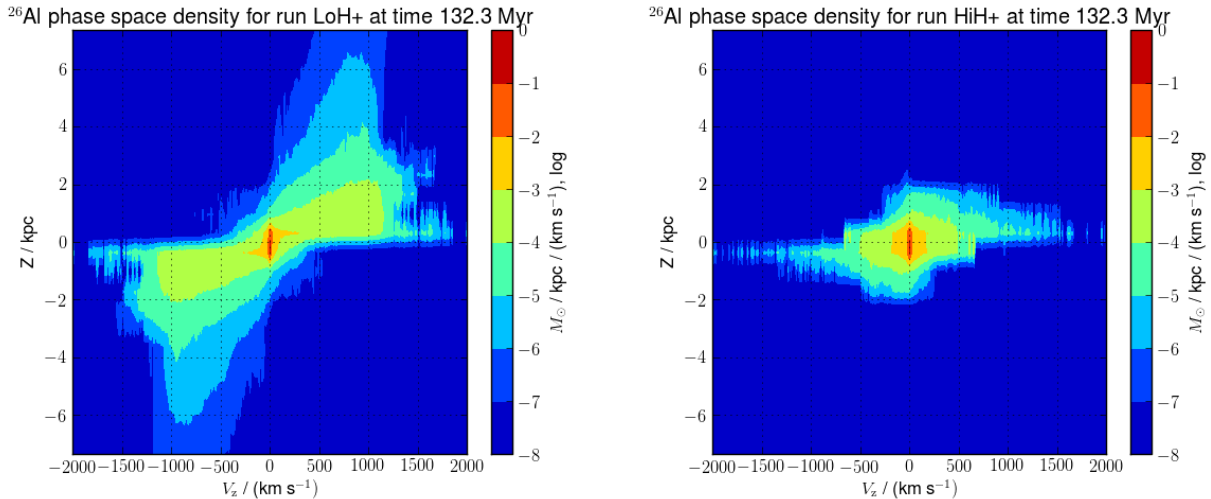


Figure 6. Phase space density for ^{26}Al for runs LoH+ (left) and HiH+ (right). Shown are 2D distributions of the coordinate vertical to the disc and the velocity in the same direction. ^{26}Al is confined by the high density halo gas in run HiH+.

be equally abundant in all galaxies, which would be in good agreement with recent LOFAR source counts (Krause et al. 2019). Much of the halo gas could also be stripped when the Milky Way will merge into the Virgo cluster (Tully et al. 2014), perhaps reinforced by simultaneous AGN triggering (Marshall et al. 2018).

Finding the metals to be distributed in roughly equal parts in cold gas and, respectively, in hot slowly cooling gas approximately 1 Myr after their ejection is in line with the extragalactic data. Observations of galaxies and galaxy clusters suggest that up to about 50 per cent of the metals remain in the galaxies (Renzini & Andreon 2014; Maiolino & Mannucci 2019). Chemodynamical simulations find a higher retained metal fraction in galaxies of higher mass, reaching 80-90 per cent for galaxies with virial masses around $10^{12}M_{\odot}$, like the Milky Way. Over cosmological timescales, some of the halo gas in the Milky Way will indeed likely cool and be re-accreted to the disc to again take part in star formation, and only a part of the enriched

halo gas will escape altogether from the dark-matter halo of the Milky Way.

6 SUMMARY AND CONCLUSIONS

We have analysed a simulation of a Milky-Way-like galaxy that traces radioactive ^{26}Al through different gas phases. ^{26}Al is a unique tracer for massive star ejecta, as it provides an additional gauge against, on one hand, INTEGRAL observations of the 1.8 MeV radioactive decay line throughout the Galaxy, and, on the other hand, against solar-system data from deposits of recent traces of massive-star ejecta and meteoritic isotopic abundance measurements for the early Solar System.

We find from our simulations that for a Milky-Way-like galaxy with superbubbles concentrated towards the spiral arms about 30-40 per cent of the ^{26}Al traced massive-star ejecta are ejected out into the

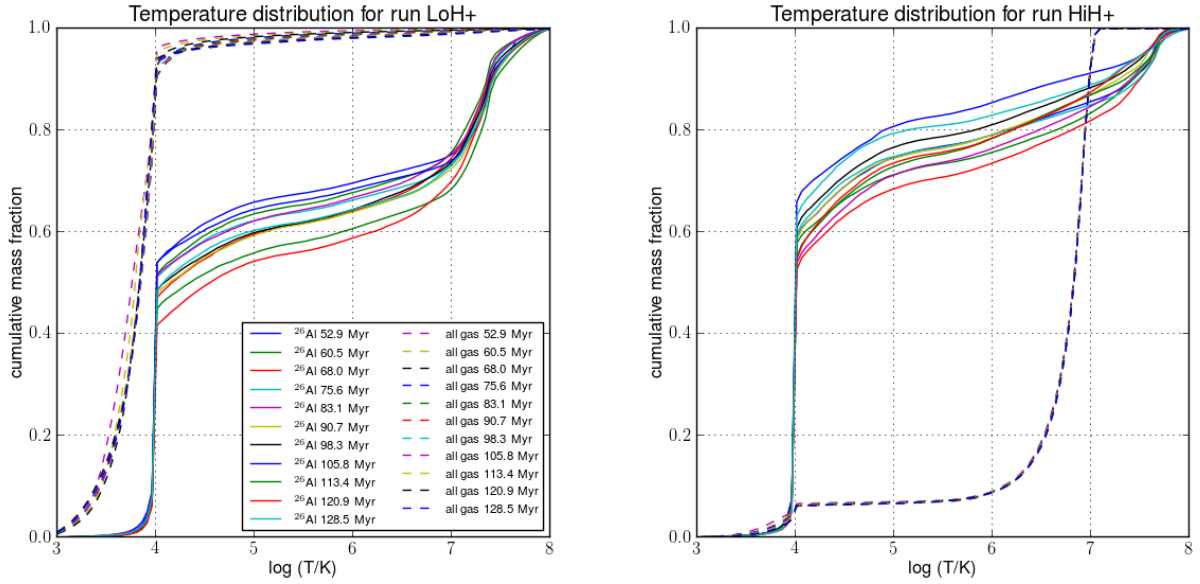


Figure 7. Temperature distributions of ^{26}Al (solid lines) and all gas (dashed lines) for typical snapshots for run LoH+ (left) and run HiH+ (right), respectively. The distributions for ^{26}Al differ significantly from the ones for all gas in both cases, with about half of the ^{26}Al being found in hot gas. The lines do not form a monotonic sequence in time, i.e., the plot shows representative random fluctuations of the distribution.

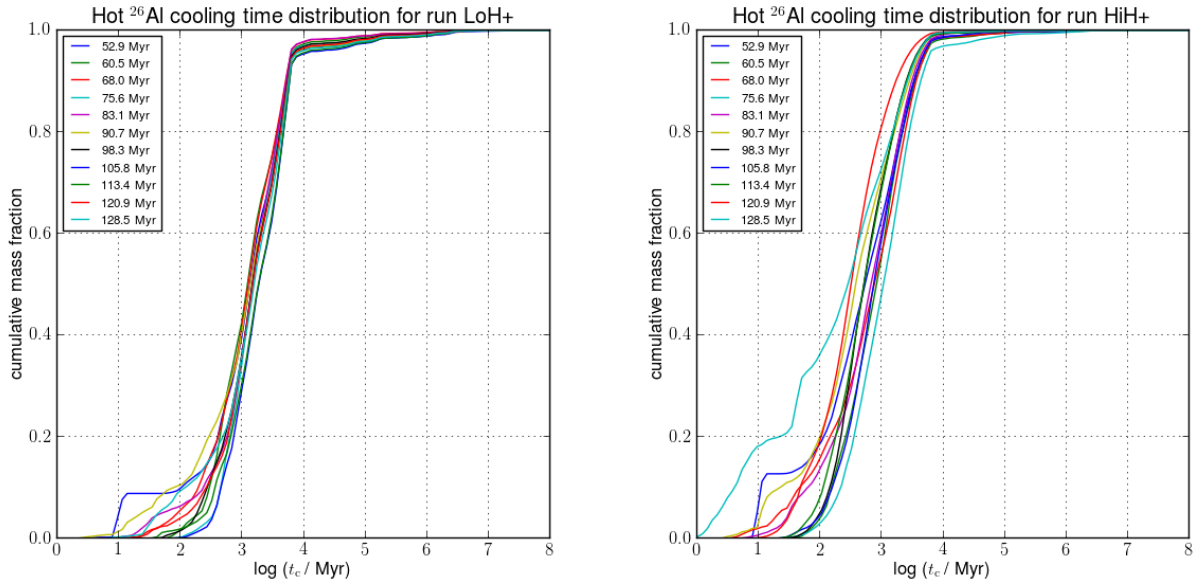


Figure 8. Cooling time distribution for ^{26}Al carrying hot gas ($T > 10^6\text{K}$) assuming solar metallicity for representative snapshots. Shown is the cumulative ^{26}Al mass over the cooling time. Almost all hot gas cooling times exceed the radioactive decay time of ^{26}Al (≈ 1 Myr) significantly.

gaseous halo at high temperatures. Even when we choke off the outflow with an unrealistically high halo density, we still get 20 per cent of the ^{26}Al into gas with temperatures above 10^6 K. Cooling times for this component are of the order of Gyr. These ejecta are therefore not immediately available for increasing the metallicity in the stellar population. The rest has diffused into gas of low temperature near our cooling limit.

These findings are in good agreement with gamma-ray data requiring a high fraction of the Galactic radioactive ^{26}Al output to

remain in hot gas. We also find a high fraction of ^{26}Al in cold gas. We do not include the formation of stars in our simulations. But in view of the results of Fujimoto et al. (2018), who also performed galaxy-scale simulations of the interstellar medium, but focussed on the diffusion of ^{26}Al into newly formed stars, a consistent view emerges: for galaxies similar to the Milky Way, metals produced by massive stars seem to branch in similar parts into cold, star forming gas and hot gas venting into the galaxy halo.

Chemodynamical cosmological simulations would require a

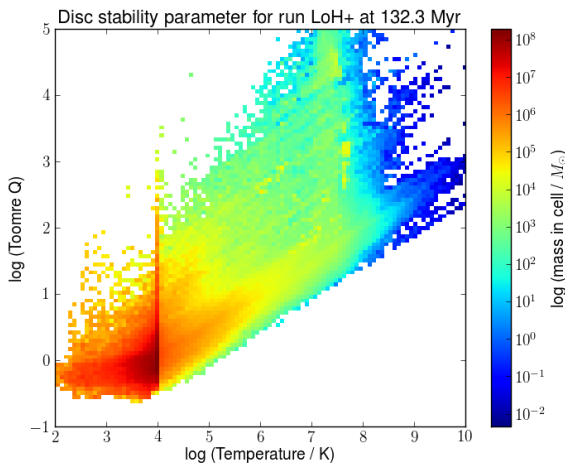


Figure 9. Two-dimensional, mass-weighted histogram of temperature and Toomre Q parameter towards the end of run LoH+ for the disc region. The cool gas generally accumulates around or just below $Q = 1$, as expected.

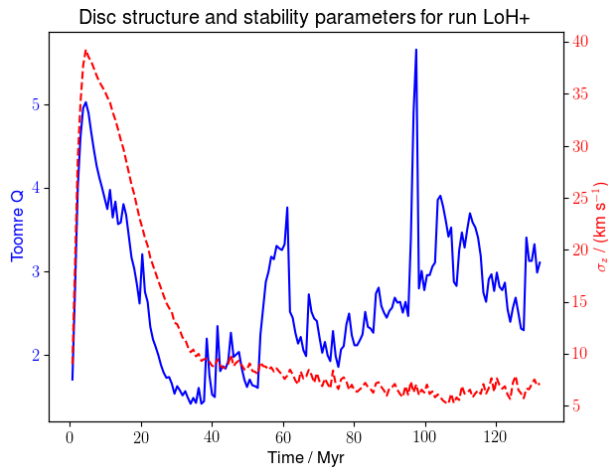


Figure 10. Run of mass weighted Toomre Q parameter and vertical velocity dispersion, σ_z over time, both for the disc region of run LoH+.

higher fraction of metals to get into stars for galaxies the size of the Milky Way over cosmological timescales. This may indicate that over much of its lifetime, these galaxies have star formation more evenly spread out in the disc and less concentrated towards the spiral arms. This would confine the outflows and likely enhance metal mixing into the cold gas, as demonstrated in run HiH+ where we confined the outflow with a high halo density. Alternatively, this may point to convective diffusion of these metals back into the Galaxy on such timescales. Overall, we find a comparable amount (within a factor of a few) of freshly produced metals in hot and cold gas respectively in our simulations, which appears remarkably similar to the ratio of metals in, respectively, stars and gas, inferred from galaxy clusters and chemical evolution modelling of galaxies.

ACKNOWLEDGEMENTS

This work has made use of the University of Hertfordshire’s high-performance computing facility. C.K. acknowledges funding from

the UK Science and Technology Facility Council (STFC) through grant ST/M000958/1 & ST/R000905/1. DRL acknowledges funding from the European Research Council (ERC) under the European Union’s Horizon 2020 research and innovation programme (grant agreement No 817540, ASTROFLOW). This article is based upon work from the “ChETEC” COST Action (CA16117), supported by COST (European Cooperation in Science and Technology). Figure 1 was produced using the visualisation tool VisIt (Childs et al. 2012). We thank the anonymous referee for useful comments that helped to improve the manuscript.

DATA AVAILABILITY

Data available on request.

REFERENCES

- Austin S. M., West C., Heger A., 2017, *ApJ*, **839**, L9
 Böhringer H., Werner N., 2010, *A&ARv*, **18**, 127
 Bouchet L., Jourdain E., Roques J.-P., 2015, *ApJ*, **801**, 142
 Breitschwerdt D., de Avillez M. A., 2006, *A&A*, **452**, L1
 Breitschwerdt D., Feige J., Schulreich M. M., Avillez M. A. D., Dettbarn C., Fuchs B., 2016, *Nature*, **532**, 73
 Brinkman H. E., Doherty C. L., Pols O. R., Li E. T., Côté B., Lugaro M., 2019, *ApJ*, **884**, 38
 Chevalier R. A., Clegg A. W., 1985, *Nature*, **317**, 44
 Childs H., et al., 2012, High Performance Visualization–Enabling Extreme-Scale Scientific Insight, pp 357–372
 Churchwell E., et al., 2006, *ApJ*, **649**, 759
 Das M., McGaugh S. S., Ianjamasimanana R., Schombert J., Dwarakanath K. S., 2020, *ApJ*, **889**, 10
 Diehl R., 2013, *Reports on Progress in Physics*, **76**, 026301
 Diehl R., et al., 1995, *A&A*, **298**, 445
 Diehl R., et al., 2006, *Nature*, **439**, 45
 Diehl R., et al., 2014, *Science*, **345**, 1162
 Dunne B. C., Points S. D., Chu Y.-H., 2001, *ApJS*, **136**, 119
 Dworkadas V. V., Dauphas N., Meyer B., Boyajian P., Bojazi M., 2017, *ApJ*, **851**, 147
 Everett J. E., Churchwell E., 2010, *ApJ*, **713**, 592
 Feige J., et al., 2018, *Phys. Rev. Lett.*, **121**, 221103
 Fujimoto Y., Krumholz M. R., Tachibana S., 2018, *MNRAS*, **480**, 4025
 Fujimoto Y., Krumholz M. R., Inutsuka S.-i., 2020, *MNRAS*, **497**, 2442
 Gaczkowski B., et al., 2015, *A&A*, **584**, A36
 Gaczkowski B., et al., 2017, *A&A*, **608**, A102
 Gounelle M., 2015, *A&A*, **582**, A26
 Gounelle M., Meynet G., 2012, *A&A*, **545**, A4
 Groopman E., et al., 2015, *ApJ*, **809**, 31
 Heath D., Krause M., Alexander P., 2007, *MNRAS*, **374**, 787
 Heckman T. M., Alexandroff R. M., Borthakur S., Overzier R., Leitherer C., 2015, *ApJ*, **809**, 147
 Iyudin A. F., et al., 1994, *A&A*, **284**, L1
 Jaskot A. E., Strickland D. K., Oey M. S., Chu Y.-H., García-Segura G., 2011, *ApJ*, **729**, 28
 Knie K., Korschinek G., Faestermann T., Dorfi E. A., Rugel G., Wallner A., 2004, *Phys. Rev. Lett.*, **93**, 171103
 Kobayashi C., Springel V., White S. D. M., 2007, *MNRAS*, **376**, 1465
 Krause M. G. H., Diehl R., 2014, *ApJ*, **794**, L21
 Krause M., Fierlinger K., Diehl R., Burkert A., Voss R., Ziegler U., 2013, *A&A*, **550**, A49
 Krause M., Diehl R., Böhringer H., Freyberg M., Lubos D., 2014, *A&A*, **566**, A94
 Krause M. G. H., et al., 2015, *A&A*, **578**, A113
 Krause M. G. H., et al., 2018, *A&A*, **619**, A120
 Krause M. G. H., Hardcastle M. J., Shabala S. S., 2019, *A&A*, **627**, A113

- Kretschmer K., Diehl R., Krause M., Burkert A., Fierlinger K., Gerhard O., Greiner J., Wang W., 2013, *A&A*, **559**, A99
- Krumholz M. R., Burkhardt B., Forbes J. C., Crocker R. M., 2018, *MNRAS*, **477**, 2716
- Lichtenberg T., Golabek G. J., Burn R., Meyer M. R., Alibert Y., Gerya T. V., Mordasini C., 2019, *Nature Astronomy*, **3**, 307
- Limongi M., Chieffi A., 2006, *ApJ*, **647**, 483
- Lugaro M., Ott U., Kereszturi Á., 2018, *Progress in Particle and Nuclear Physics*, **102**, 1
- MacPherson G. J., Bullock E. S., Janney P. E., Kita N. T., Ushikubo T., Davis A. M., Wadhwa M., Krot A. N., 2010, *ApJ*, **711**, L117
- Mackey J., Gvaramadze V. V., Mohamed S., Langer N., 2015, *A&A*, **573**, A10
- Maiolino R., Mannucci F., 2019, *A&ARv*, **27**, 3
- Marshall M. A., Shabala S. S., Krause M. G. H., Pimblet K. A., Croton D. J., Owers M. S., 2018, *MNRAS*, **474**, 3615
- Nomoto K., Kobayashi C., Tominaga N., 2013, *ARA&A*, **51**, 457
- Oey M. S., García-Segura G., 2004, *ApJ*, **613**, 302
- Orr M. E., et al., 2020, *MNRAS*, **496**, 1620
- Pettitt A. R., Ragan S. E., Smith M. C., 2020, *MNRAS*, **491**, 2162
- Pleintinger M. M. M., Siebert T., Diehl R., Fujimoto Y., Greiner J., Krause M. G. H., Krumholz M. R., 2019, arXiv e-prints, p. [arXiv:1910.06112](https://arxiv.org/abs/1910.06112)
- Plüschke S., et al., 2001, in Gimenez A., Reglero V., Winkler C., eds, ESA Special Publication Vol. 459, Exploring the Gamma-Ray Universe. pp 55–58 ([arXiv:astro-ph/0104047](https://arxiv.org/abs/astro-ph/0104047))
- Portegies Zwart S., 2019, *A&A*, **622**, A69
- Prantzos N., Diehl R., 1996, *Phys. Rep.*, **267**, 1
- Renaud M., et al., 2006, *ApJ*, **647**, L41
- Renzini A., Andreon S., 2014, *MNRAS*, **444**, 3581
- Rodgers-Lee D., Krause M. G. H., Dale J., Diehl R., 2019, *MNRAS*, **490**, 1894
- Rogers H., Pittard J. M., 2013, *MNRAS*, **431**, 1337
- Sasaki M., Breitschwerdt D., Baumgartner V., Haberl F., 2011, *A&A*, **528**, A136+
- Schulreich M., Breitschwerdt D., Feige J., Dettbarn C., 2018, *Galaxies*, **6**, 26
- Sellwood J. A., Trick W. H., Carlberg R. G., Coronado J., Rix H.-W., 2019, *MNRAS*, **484**, 3154
- Simionescu A., et al., 2019, *MNRAS*, **483**, 1701
- Sutherland R. S., Dopita M. A., 1993, *ApJS*, **88**, 253
- Taylor P., Kobayashi C., 2015, *MNRAS*, **452**, L59
- Toomre A., 1964, *ApJ*, **139**, 1217
- Tully R. B., Courtois H., Hoffman Y., Pomarède D., 2014, *Nature*, **513**, 71
- Wallner A., et al., 2015, *Nature Communications*, **6**, 5956
- Wang W., et al., 2007, *A&A*, **469**, 1005
- Wang W., et al., 2020, *ApJ*, **889**, 169
- Weaver R., McCray R., Castor J., Shapiro P., Moore R., 1977, *ApJ*, **218**, 377
- Woosley S. E., Heger A., 2007, *Phys. Rep.*, **442**, 269
- Zinnecker H., Yorke H. W., 2007, *ARA&A*, **45**, 481
- de Avillez M. A., Breitschwerdt D., 2004, *A&A*, **425**, 899
- von Glasow W., Krause M. G. H., Sommer-Larsen J., Burkert A., 2013, *MNRAS*, **434**, 1151

This paper has been typeset from a $\text{\TeX}/\text{\LaTeX}$ file prepared by the author.